

Ab initio predictions link the neutron skin of ^{208}Pb to nuclear forces

Baishan Hu,^{1,*} Weiguang Jiang,^{2,*} Takayuki Miyagi,^{1,3,*} Zhonghao Sun,^{4,5,*} Andreas Ekström,² Christian Forssén,^{2,†} Gaute Hagen,^{5,4,1} Jason D. Holt,^{1,6} Thomas Papenbrock,^{4,5} S. Ragnar Stroberg,^{7,8} and Ian Vernon⁹

¹TRIUMF, 4004 Wesbrook Mall, Vancouver, BC V6T 2A3, Canada

²Department of Physics, Chalmers University of Technology, SE-412 96 Göteborg, Sweden

³Technische Universität Darmstadt, Department of Physics, 64289 Darmstadt, Germany

⁴Department of Physics and Astronomy, University of Tennessee, Knoxville, Tennessee 37996, USA

⁵Physics Division, Oak Ridge National Laboratory, Oak Ridge, Tennessee 37831, USA

⁶Department of Physics, McGill University, 3600 Rue University, Montréal, QC H3A 2T8, Canada

⁷Department of Physics, University of Washington, Seattle, Washington 98195, USA

⁸Physics Division, Argonne National Laboratory, Lemont, Illinois 60439, USA

⁹Department of Mathematical Sciences, University of Durham, South Road, Durham, DH1 3LE, UK

Heavy atomic nuclei have an excess of neutrons over protons. This leads to the formation of a neutron skin whose thickness, R_{skin} , is sensitive to details of the nuclear force—linking atomic nuclei to properties of neutron stars, thereby relating objects that differ in size by 18 orders of magnitude [1, 2]. ^{208}Pb is of particular interest here because it exhibits a simple structure and is accessible to experiment. However, computing such a heavy nucleus has been out of reach for *ab initio* theory. By combining advances in quantum many-body methods, statistical tools, and emulator technology, we make quantitative predictions for the properties of ^{208}Pb starting from nuclear forces that are consistent with symmetries of low-energy quantum chromodynamics. We explore 10^9 different nuclear-force parameterisations via history matching, confront them with data in select light nuclei, and arrive at an importance-weighted ensemble of interactions. We accurately reproduce bulk properties of ^{208}Pb and find $R_{\text{skin}}(^{208}\text{Pb}) = 0.14 - 0.20$ fm which is smaller than a recent extraction from parity-violating electron scattering [3] but in agreement with other experimental probes. The allowable range of $R_{\text{skin}}(^{208}\text{Pb})$ is significantly constrained by nucleon-nucleon scattering data, ruling out very thick skins. This work demonstrates that nuclear forces constrained to light systems extrapolate reliably to even the heaviest nuclei, and that we can make quantitative predictions across the nuclear landscape.

Introduction

Neutron stars are extreme astrophysical objects whose interiors may contain exotic new forms of matter. The structure and size of neutron stars are linked to the thickness of neutron skins in atomic nuclei via the neutron-matter equation of state [1, 2, 4]. The nucleus ^{208}Pb is an attractive target for exploring this link in both experimental [3, 5] and theoretical [2, 6, 7] studies, due to the large excess of neutrons and its simple structure. Mean-field calculations predict a wide range for $R_{\text{skin}}(^{208}\text{Pb})$ because the isovector parts of nuclear energy density functionals are not well constrained [7]. Additional constraints may be obtained [8] by including the electric dipole polarisability of ^{208}Pb , though this comes with a model dependence [9] which is difficult to quantify. In contrast, a narrower range of neutron skins has been predicted for the medium-mass nucleus ^{48}Ca by *ab initio* computations [10] based on various sets of two- and three-nucleon forces. Due to breakthrough developments in quantum many-body methods, such computations are now feasible for heavy nuclei [11–14]. The *ab initio* computation of ^{208}Pb reported in this paper represents a significant step in mass number from the previously computed tin isotopes [11, 12], as illustrated in

Figure 1. The complementary statistical analysis in this work is enabled by emulators (for mass number $A \leq 16$) which mimic the outputs of many-body solvers, but are orders of magnitude faster.

Our approach to constructing nuclear interactions is based on chiral effective field theory (EFT) [16–18]. In this theory the long-range part of the strong nuclear force is known and stems from pion exchanges, while the unknown short-range contributions are represented as contact interactions; we also include the Δ isobar degree of freedom [19]. At next-to-next-to leading order in Weinberg’s power counting, the four pion-nucleon low-energy constants (LECs) are tightly fixed from pion-nucleon scattering data[20]. The 13 additional LECs in the nuclear potential must be constrained from data. In this paper we develop a unified *ab initio* framework to link the physics of nucleon-nucleon scattering and few-nucleon systems to properties of medium- and heavy-mass nuclei up to ^{208}Pb , and ultimately to the nuclear matter equation of state near saturation density.

Linking models to reality

We use history matching [21, 22] to iteratively identify a *non-implausible* region in the vast parameter space of LECs for which the output of *ab initio* methods yield acceptable agreement with selected experimental data—here denoted history-matching observables. The key to

* contributed equally

† corresponding author: christian.forssen@chalmers.se

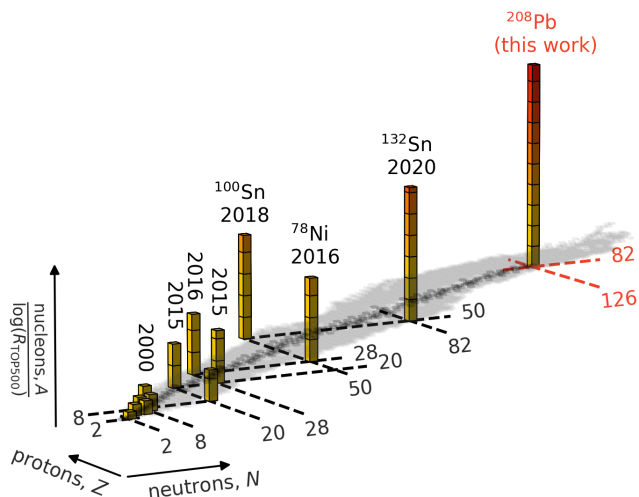


Figure 1 | Trend of realistic *ab initio* computations for the nuclear A -body problem. The bars highlight years of first realistic computations of doubly magic nuclei. The height of each bar corresponds to the mass number A divided by the logarithm of the total compute power (in flop/second) of the pertinent TOP500 list [15]. This ratio would be approximately constant if progress were solely due to exponentially increasing computing power. However, algorithms which instead scale polynomially in A have greatly increased the reach.

efficiently analyze this high-dimensional parameter space is the use of emulators based on eigenvector continuation [23–25] that accurately mimic the outputs of the *ab initio* methods at several orders of magnitude lower computational cost. We consider the following history-matching observables: nucleon-nucleon scattering phase shifts up to an energy of 200 MeV; the energy, radius, and quadrupole moment of ^2H ; and the energies and radii of ^3H , ^4He , and ^{16}O . We perform five waves of this global parameter search—sequentially ruling out implausible LECs that yield model predictions too far from experimental data. For this purpose we use an implausibility measure (see Methods) that links our model predictions and experimental observations as

$$z = M(\theta) + \varepsilon_{\text{exp}} + \varepsilon_{\text{em}} + \varepsilon_{\text{method}} + \varepsilon_{\text{model}}. \quad (1)$$

Here, experimental observations, z , are related to emulated *ab initio* predictions $M(\theta)$ via random variables ε_{exp} , ε_{em} , $\varepsilon_{\text{method}}$, $\varepsilon_{\text{model}}$ that represent experimental uncertainties, emulator precision, method approximation errors, and the model discrepancy due to the EFT truncation at next-to-next-to leading order, respectively. The parameter vector θ corresponds to the 17 LECs at this order. The method error represents, e.g., model-space truncations and other approximations in the employed *ab initio* many-body solvers. The model discrepancy $\varepsilon_{\text{model}}$ can be probabilistically specified since we assume to op-

erate with an order-by-order improvable EFT description of the nuclear interaction (see Methods for details).

The final result of the five history-matching waves is a set of 34 non-implausible samples in the 17-dimensional parameter space of the LECs. We then perform *ab initio* calculations for nuclear observables in ^{48}Ca and ^{208}Pb , as well as for properties of infinite nuclear matter.

Ab initio computations of ^{208}Pb

We employ the coupled-cluster (CC) [26–28] and the in-medium similarity renormalization group (IMSRG) [29] methods to approximately solve the Schrödinger equation and obtain the ground-state energy and nucleon densities of ^{48}Ca and ^{208}Pb . We analyze the model-space convergence of the solutions and quantify the differences between CC and IMSRG results to estimate the method approximation errors. The computational cost of these methods scales (only) polynomially with increasing numbers of nucleons and single-particle orbitals. The main challenge in computing ^{208}Pb is the vast number of matrix elements of the three-nucleon force which must be handled. We overcome this limitation by using a recently introduced storage scheme in which we only store linear combinations of matrix elements directly entering the normal-ordered two-body approximation [14] (see Methods for details).

Our *ab initio* predictions for finite nuclei are summarized in Figure 2. The statistical approach that leads to these results is composed of three stages. First, history matching identified a set of 34 non-implausible interaction parametrizations. Second, model calibration is performed by weighting these parametrizations—serving as prior samples—using a likelihood measure according to the principles of sampling/importance resampling[33]. This yields 34 weighted samples from the LEC posterior probability density function. Specifically we assume independent EFT and many-body method errors and construct a normally distributed data-likelihood encompassing the ground-state energy per nucleon E/A and point-proton radius R_p for ^{48}Ca , and the energy E_{2^+} of its first excited 2^+ state. We have tested the sensitivity of final results to the likelihood definition by repeating the calibration with a non-diagonal covariance matrix or a Student-t distribution with heavier tails, finding small ($\sim 1\%$) differences in the predicted credible regions. The EFT truncation errors are quantified by studying *ab initio* predictions at different orders in the power counting for ^{48}Ca and infinite nuclear matter. We validate our *ab initio* model and error assignments by computing the posterior predictive distributions, including all relevant sources of uncertainty, for both the replicated calibration data (blue colour) and the history-matching observables (green colour), see Figure 2. The percentage ratios $\sigma_{\text{tot}}/\mathcal{O}_{\text{exp}}$ of the (theory dominated) total uncertainty to the experimental value are given in the right margin.

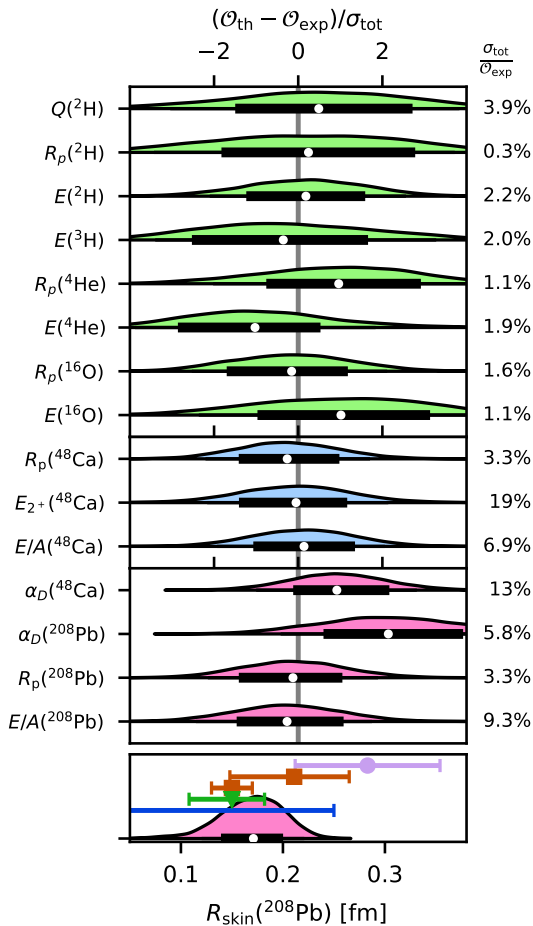


Figure 2 | *Ab initio* posterior predictive distributions for light to heavy nuclei. Model checking is indicated by green and blue distributions, corresponding to observables used for history-matching and likelihood calibration, respectively, while pure predictions are shown as pink distributions. See text and Extended Data Table 1 for detailed numerical specification of experimental data (\mathcal{O}_{exp}), incorporated errors (σ_{tot}) and numerical credibility regions. The prediction for $R_{\text{skin}}(^{208}\text{Pb})$ in the bottom panel is shown in an absolute scale and compared to experimental results using different probes: electroweak [3] (purple), hadronic [30, 31] (red), electromagnetic [5] (green), and gravitational waves [32] (blue) (from top to bottom).

Finally, having built confidence in our *ab initio* model and underlying assumptions, we predict $R_{\text{skin}}(^{208}\text{Pb})$, E/A and R_{ρ} for ^{208}Pb , as well as α_D for ^{48}Ca and ^{208}Pb , by employing importance resampling [33]. The corresponding posterior predictive distributions are shown in the lower panels of Figure 2 (pink colour). Our prediction $R_{\text{skin}}(^{208}\text{Pb}) = 0.14 - 0.20$ fm exhibits a mild tension with the value extracted from the recent parity-violating electron scattering experiment PREX [3] but is consistent with the skin thickness extracted from elastic proton scattering [31], antiprotonic atoms [30] and coherent pion

photoproduction [5] as well as constraints from gravitational waves from merging neutron stars [32].

We also compute the weak form factor $F_w(Q^2)$ at momentum transfer $Q_{\text{PREX}} = 0.3978(16)$ fm $^{-1}$, which is more directly related to the parity-violating asymmetry measured in the PREX experiment. We observe a strong correlation with the more precisely measured electric charge form factor $F_{\text{ch}}(Q^2)$, as shown in Figure 3b. While we have not quantified the EFT and method errors for these observables, we find a small variance among the 34 non-implausible predictions for the difference $F_w(Q^2) - F_{\text{ch}}(Q^2)$ for both ^{48}Ca and ^{208}Pb as shown in Figure 3c.

Ab initio computations of infinite nuclear matter

The nuclear matter equation of state and saturation properties are computed with the CC method in the CCD(T) approximation on a momentum-space lattice with periodic boundary conditions [34]. We employ a Bayesian machine-learning error model [35] to quantify the uncertainties. This allows us to incorporate correlations between the EFT truncation errors. We used the same approach to also learn about the CC method uncertainties as a function of nuclear-matter density (see Methods for details).

The posterior predictive distributions for observables related to the nuclear equation of state at saturation density are shown in Figure 3a. These distributions include samples from the relevant method and model error terms. Overall, we reveal relevant correlations among observables, previously indicated in mean-field models, and find good agreement with empirical bounds [36]. The last row shows the resulting correlations with $R_{\text{skin}}(^{208}\text{Pb})$ in our *ab initio* framework. Depending on our assumptions about the model error, these correlations are less pronounced than indicated by density functional theory.

Discussion

Ab initio computations predict a relatively small neutron-skin thickness for both ^{208}Pb and ^{48}Ca , see Extended Data Table 2 and Ref. [10]. For ^{208}Pb our narrow predicted range of neutron skins is consistent with several extractions [5, 37, 38] (each of which involves some model-dependence) and in mild tension (approximately at the 1.5σ level) with the recent PREX result [3]. In contrast, phenomenological mean-field models can accommodate a large skin while still reproducing experimental binding energies and charge radii of medium- and heavy-mass nuclei [7]. One is naturally led to ask whether this is because the *ab initio* calculations incorporate additional constraining information from, e.g., scattering data, or because our EFT-based model for nuclear interactions is not sufficient to describe the relevant physics. We shall

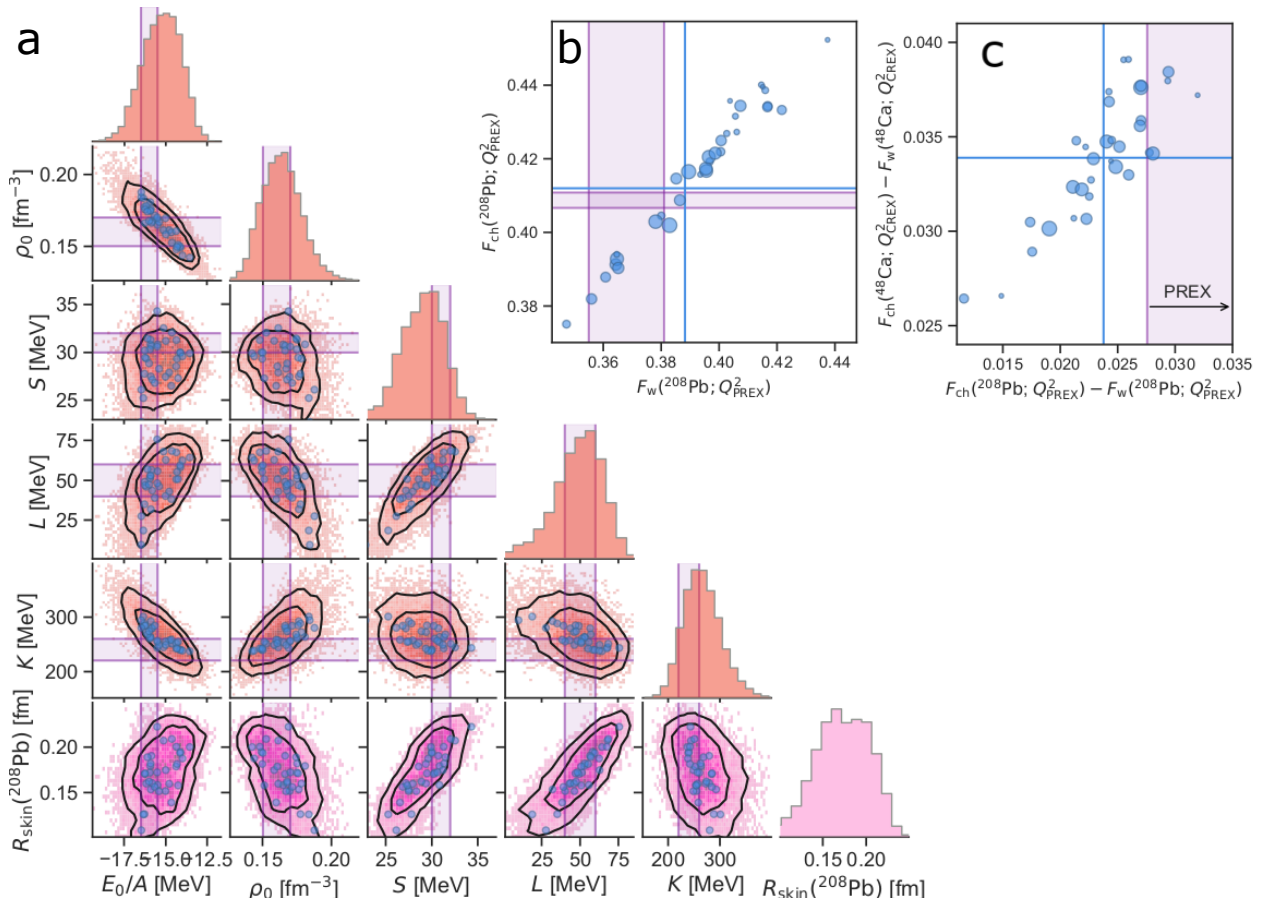


Figure 3 | Posterior predictive distribution for $R_{\text{skin}}(^{208}\text{Pb})$ and nuclear matter at saturation density. **a**, Predictions for the saturation density ρ_0 of symmetric nuclear matter, its compressibility K , the symmetry energy S , and its slope L are correlated with the those for $R_{\text{skin}}(^{208}\text{Pb})$. The bivariate distribution include 68% and 90% credible regions (black lines) and a scatter plot of the predictions with the 34 non-implausible samples before error sampling. Empirical nuclear-matter properties are indicated by purple bands. **b**, Predictions with the 34 non-implausible samples for the electric versus weak charge form factors for ^{208}Pb at the momentum transfer considered in the PREX experiment [3]. **c**, Difference between electric and weak charge form factors for ^{48}Ca and ^{208}Pb at the momentum transfers $Q_{\text{CREX}} = 0.873 \text{ fm}^{-1}$ and $Q_{\text{PREX}} = 0.3798 \text{ fm}^{-1}$ that are relevant for the CREX and PREX experiments, respectively. Experimental data (purple bands) in panels b and c are from Ref. [3], the size of the markers indicate the importance weight, and blue lines correspond to weighted means.

argue in favor of the former.

The large variation in neutron skins obtained in mean-field calculations directly corresponds to a large variation in the equation of state of pure neutron matter [1, 39]. Neutron matter below saturation density ρ_0 is fairly well constrained by nucleon-nucleon scattering data [35, 40, 41]. Indeed, we find that $R_{\text{skin}}(^{208}\text{Pb})$ correlates with information from scattering data, with the strongest correlation in the 1S_0 partial wave for laboratory energies around 50 MeV (naively corresponding to the Fermi energy of neutron matter at $0.8\rho_0$), see Extended Data Figure 7. While it is possible to increase the slope L of the symmetry energy beyond the range predicted in this work—by tuning a contact in the 1S_0 partial wave and readjusting the three-body contact to maintain realistic nuclear saturation—we find that re-

production of the 1S_0 scattering phase shifts deteriorates (see Extended Data Figure 8). Analogous freedom exists in mean field theory. In non-relativistic Skyrme parameterisations [42] the slope L can be modified by changing the parameter that controls the isospin dependence of the S -wave contact interaction while readjusting the parameter of the three-nucleon force to preserve saturation (see Extended Data Figure 8 and Ref. [1]). In the relativistic framework, one may tune the equation of state in a similar fashion by modifying the coupling of the isovector meson to nucleons while compensating with a non-linear meson coupling [43] (which effectively modifies the density dependence of the two-nucleon interaction[39]). The essential point is that mean-field calculations are not directly confronted with scattering data, leaving L and (correspondingly R_{skin}) largely unconstrained.

Moving forward, it will be important to extend these calculations to higher orders in the effective field theory, to further validate the error model and improve precision. The framework presented in this work will enable predictions with quantified uncertainties across the nuclear chart. The confrontation between theory and data in such a framework promises to relate the properties of strongly interacting and complex many-body systems, such as atomic nuclei as well as the interiors of neutron stars, to the forces between two and three nucleons.

-
- [1] B. Alex Brown, Phys. Rev. Lett. **85**, 5296 (2000).
 [2] C. J. Horowitz and J. Piekarewicz, Phys. Rev. Lett. **86**, 5647 (2001).
 [3] D. Adhikari *et al.* (PREX), Phys. Rev. Lett. **126**, 172502 (2021).
 [4] R. Essick, I. Tews, P. Landry, and A. Schwenk, Phys. Rev. Lett. **127**, 192701 (2021).
 [5] C. M. Tarbert *et al.*, Phys. Rev. Lett. **112**, 242502 (2014).
 [6] M. B. Tsang, J. R. Stone, F. Camera, P. Danielewicz, S. Gandolfi, K. Hebeler, C. J. Horowitz, J. Lee, W. G. Lynch, Z. Kohley, R. Lemmon, P. Möller, T. Murakami, S. Riordan, X. Roca-Maza, F. Sammarruca, A. W. Steiner, I. Vidaña, and S. J. Yennello, Phys. Rev. C **86**, 015803 (2012).
 [7] X. Roca-Maza, M. Centelles, X. Viñas, and M. Warda, Phys. Rev. Lett. **106**, 252501 (2011).
 [8] P.-G. Reinhard, X. Roca-Maza, and W. Nazarewicz, Phys. Rev. Lett. **127**, 232501 (2021).
 [9] J. Piekarewicz, B. K. Agrawal, G. Colò, W. Nazarewicz, N. Paar, P.-G. Reinhard, X. Roca-Maza, and D. Vretenar, Phys. Rev. C **85**, 041302 (2012).
 [10] G. Hagen, A. Ekström, C. Forssén, G. R. Jansen, W. Nazarewicz, T. Papenbrock, K. A. Wendt, S. Bacca, N. Barnea, B. Carlsson, C. Drischler, K. Hebeler, M. Hjorth-Jensen, M. Miorelli, G. Orlandini, A. Schwenk, and J. Simonis, Nature Physics **12**, 186 (2016).
 [11] T. D. Morris, J. Simonis, S. R. Stroberg, C. Stumpf, G. Hagen, J. D. Holt, G. R. Jansen, T. Papenbrock, R. Roth, and A. Schwenk, Phys. Rev. Lett. **120**, 152503 (2018).
 [12] P. Arthuis, C. Barbieri, M. Vorabbi, and P. Finelli, Phys. Rev. Lett. **125**, 182501 (2020).
 [13] S. R. Stroberg, J. D. Holt, A. Schwenk, and J. Simonis, Phys. Rev. Lett. **126**, 022501 (2021).
 [14] T. Miyagi, S. R. Stroberg, P. Navrátil, K. Hebeler, and J. D. Holt, (2021), arXiv:2104.04688 [nucl-th].
 [15] “TOP500 Statistics,” <https://www.top500.org/statistics/perfdevel/>, accessed Nov. 1, 2021.
 [16] E. Epelbaum, H.-W. Hammer, and U.-G. Meißner, Rev. Mod. Phys. **81**, 1773 (2009).
 [17] R. Machleidt and D. Entem, Phys. Rep. **503**, 1 (2011).
 [18] H. W. Hammer, S. König, and U. van Kolck, Rev. Mod. Phys. **92**, 025004 (2020).
 [19] C. Ordóñez, L. Ray, and U. van Kolck, Phys. Rev. C **53**, 2086 (1996).
 [20] M. Hoferichter, J. Ruiz de Elvira, B. Kubis, and U.-G. Meißner, Phys. Rev. Lett. **115**, 192301 (2015).
 [21] I. Vernon, M. Goldstein, and R. G. Bower, Bayesian Anal. **5**, 619 (2010).
 [22] I. Vernon, M. Goldstein, and R. Bower, Statist. Sci. **29**, 81 (2014).
 [23] D. Frame, R. He, I. Ipsen, D. Lee, D. Lee, and E. Rrapaj, Phys. Rev. Lett. **121**, 032501 (2018).
 [24] S. König, A. Ekström, K. Hebeler, D. Lee, and A. Schwenk, Phys. Lett. B **810**, 135814 (2020).
 [25] A. Ekström and G. Hagen, Phys. Rev. Lett. **123**, 252501 (2019).
 [26] H. Kümmel, K. H. Lührmann, and J. G. Zabolitzky, Physics Reports **36**, 1 (1978).
 [27] R. J. Bartlett and M. Musiał, Rev. Mod. Phys. **79**, 291 (2007).
 [28] G. Hagen, T. Papenbrock, M. Hjorth-Jensen, and D. J. Dean, Rep. Prog. Phys. **77**, 096302 (2014).
 [29] H. Hergert, S. K. Bogner, T. D. Morris, A. Schwenk, and K. Tsukiyama, Phys. Rep. **621**, 165 (2016).
 [30] A. Trzcinska, J. Jastrzebski, P. Lubinski, F. J. Hartmann, R. Schmidt, T. von Egidy, and B. Klos, Phys. Rev. Lett. **87**, 082501 (2001).
 [31] J. Zenihiro, H. Sakaguchi, T. Murakami, M. Yosoi, Y. Yasuda, S. Terashima, Y. Iwao, H. Takeda, M. Itoh, H. P. Yoshida, and M. Uchida, Phys. Rev. C **82**, 044611 (2010).
 [32] F. J. Fattoyev, J. Piekarewicz, and C. J. Horowitz, Phys. Rev. Lett. **120**, 172702 (2018).
 [33] A. F. M. Smith and A. E. Gelfand, Am. Stat. **46**, 84 (1992).
 [34] G. Hagen, T. Papenbrock, A. Ekström, K. A. Wendt, G. Baardsen, S. Gandolfi, M. Hjorth-Jensen, and C. J. Horowitz, Phys. Rev. C **89**, 014319 (2014).
 [35] C. Drischler, R. J. Furnstahl, J. A. Melendez, and D. R. Phillips, Phys. Rev. Lett. **125**, 202702 (2020).
 [36] J. M. Lattimer and Y. Lim, Ap. J. **771**, 51 (2013).
 [37] L. Ray, Phys. Rev. C **19**, 1855 (1979).
 [38] X. Roca-Maza, X. Viñas, M. Centelles, B. K. Agrawal, G. Colò, N. Paar, J. Piekarewicz, and D. Vretenar, Phys. Rev. C **92**, 064304 (2015).
 [39] S. Typel and B. A. Brown, Phys. Rev. C **64**, 27302 (2001).
 [40] C. J. Pethick and D. G. Ravenhall, Annu. Rev. Nucl. Part. Sci. **45**, 429 (1995).
 [41] I. Tews, J. M. Lattimer, A. Ohnishi, and E. E. Kolomeitsev, Astrophys. J. **848**, 105 (2017).
 [42] B. A. Brown, Phys. Rev. C **58**, 220 (1998).
 [43] B. G. Todd-Rutel and J. Piekarewicz, Phys. Rev. Lett. **95**, 122501 (2005).

Methods

Hamiltonian and model-space

The many-body approaches used in this work [CC, IMSRG, and many-body perturbation theory (MBPT)] start from the intrinsic Hamiltonian

$$H = T_{\text{kin}} - T_{\text{CoM}} + V_{\text{NN}} + V_{\text{3N}}. \quad (2)$$

Here T_{kin} is the kinetic energy, T_{CoM} is the kinetic energy of the center of mass, V_{NN} is the nucleon-nucleon, and V_{3N} is the three-nucleon interaction. In order to facilitate the convergence of heavy nuclei, the interac-

tions employed in this work used a non-local regulator with a cutoff $\Lambda = 394$ MeV/ c . Results should be independent of this choice, up to higher-order corrections, provided renormalization-group invariance of the EFT. However, increasing the momentum scale of the cutoff leads to harder interactions, considerably enlarging the required computational effort. We represent the 34 non-implausible interactions that resulted from the history-matching analysis in the Hartree-Fock basis in a model-space of up to 15 major harmonic oscillator shells ($e = 2n + l \leq e_{\max} = 14$ where n and l denote the radial and orbital angular momentum quantum numbers, respectively) with oscillator frequency $\hbar\omega = 10$ MeV. Due to storage limitations, the three-nucleon force had an additional energy cut given by $e_1 + e_2 + e_3 \leq E_{3\max} = 28$. After obtaining the Hartree-Fock basis for each of the 34 non-implausible interactions, we capture 3N force effects via the normal-ordered two-body approximation before proceeding with the CC, IMSRG and MBPT calculations [44, 45]. The convergence behaviour in e_{\max} and $E_{3\max}$ is illustrated in Extended Data Figure 1. In that figure, we use an interaction with a high likelihood that generates a large correlation energy. Thus, its convergence behaviour represents the worst case among the 34 non-implausible interactions. We estimate that extrapolating to $e_{\max} \rightarrow \infty$, $E_{3\max} \rightarrow 3e_{\max}$ will shift the energy results in the model space $e_{\max} = 14$, $E_{3\max} = 28$ by -75 ± 60 MeV. Likewise, we estimate that extrapolating will shift the neutron skin by $+0.005 \pm 0.010$ fm.

In-medium similarity renormalization group calculations

The IMSRG calculations [29],[46] were performed at the IMSRG(2) level, using the Magnus formulation [47]. Operators for the point-proton and point-neutron radii, form factors, and the electric dipole operator were consistently transformed. The dipole polarizability α_D was computed using the equations-of-motion method truncated at the 2-particle-2-hole level (the EOM-IMSRG(2,2) approximation [48]) and the Lanczos continued fraction method [49]. We compute the weak and charge form factors using the parameterization presented in Ref. [50], though the form given in Ref. [51] yields nearly identical results.

Many-body perturbation theory calculations

MBPT theory calculations for ^{208}Pb were performed in the Hartree-Fock basis to third order for the energies, and to second order for radii.

Coupled-cluster calculations

The CC calculations of ^{208}Pb were truncated at the singles-and-doubles excitation level, known as the CCSD approximation [26–28]. We estimated the contribution from triples excitations to the ground-state energy of ^{208}Pb as 10% of the CCSD correlation energy (which is a reliable estimate for closed-shell systems [27]).

Extended Data Figure 3 compares the different many-body approaches used in this work, i.e. CC, IMSRG, MBPT, and allows us to estimate the uncertainties related to our many-body approach in computing the ground-state observables for ^{208}Pb . The point proton and neutron radii are computed as ground-state expectation values (see e.g. Ref. [10] for details). For ^{48}Ca we used a Hartree-Fock basis consisting of 15 major oscillator shells with an oscillator spacing of $\hbar\omega = 16$ MeV, while for 3N forces we used $E_{3\max} = 16$, which is sufficiently large to obtain converged results in this mass region. Here we computed the ground-state energy using the Λ -CCSD(T) approximation [52] which include perturbative triples corrections. The 2^+ excited state in ^{48}Ca was computed using the equation-of-motion CCSD approach [53], and we estimated a -1 MeV shift from triples excitations based on EOM-CCSD(T) calculations of ^{48}Ca and ^{78}Ni using similar interactions [54].

For the history-matching analysis we used an emulator for the ^{16}O ground-state energy and charge radius that was constructed using the recently developed sub-space coupled-cluster method [25]. For higher precision in the emulator we went beyond the SP-CCSD approximation used in Ref. [25] and included leading-order triples excitations via the CCSDT-3 method [55]. The CCSDT-3 ground-state training vectors for ^{16}O were obtained starting from the Hartree-Fock basis of the recently developed chiral interaction $\Delta\text{NNLO}_{\text{GO}}(394)$ of Ref. [56] in a model-space consisting of 11 major harmonic oscillator shells with the oscillator frequency $\hbar\omega = 16$ MeV, and $E_{3\max} = 14$. The emulator used in the history matching was constructed by selecting 68 different training points in the 17-dimensional space of LECs using a space-filling Latin hypercube design in a 10% variation around the $\Delta\text{NNLO}_{\text{GO}}(394)$ LECs. At each training point we then performed a CCSDT-3 calculation in order to obtain the training vectors for which we then construct the sub-space projected norm and Hamiltonian matrices. Once the SP-CCSDT-3 matrices are constructed we may obtain the ground-state energy and charge radii for any target values of the LECs by diagonalizing a 68 by 68 generalized eigenvalue problem (see Ref. [25] for more details). We checked the accuracy of the emulator by cross-validation against full-space CCSDT-3 calculations as demonstrated in Extended Data Figure 2 and found a relative error that was smaller than 0.2%.

The nuclear matter equation of state and saturation properties are computed with the CCD(T) approximation which includes doubles excitations and perturbative

triples corrections. The three-nucleon forces are considered beyond the normal-ordered two-body approximation by including the residual three-nucleon force contribution in the triples. The calculations are performed on a cubic lattice in momentum space with periodic boundary conditions. The model space is constructed with $(2n_{\max} + 1)^3$ momentum points, and we use $n_{\max} = 4(3)$ for pure neutron matter (symmetric nuclear matter) and obtain converged results. We perform calculations for systems of 66 neutrons (132 nucleons) for pure neutron matter (symmetric nuclear matter) since results obtained with those particle numbers exhibit small finite size effects [34].

Iterative history matching

In this work we use an iterative approach known as history matching [21, 22] in which the model, solved at different fidelities, is confronted with experimental data z using relation (1). Obviously, we do not know the exact values of the errors in Eq. (1), hence we represent them as uncertain quantities and specify reasonable forms for their statistical distributions, in alignment with the Bayesian paradigm.

We employ quantified method and emulator errors as discussed above. Probabilistic attributes of the model discrepancy terms are assigned based on the expected EFT convergence pattern [57, 58]. For the history-matching observables considered here we use point estimates of model errors from Ref. [59].

The aim of history matching is to estimate the set $\mathcal{Q}(z)$ of parameterizations θ , for which the evaluation of a model $M(\theta)$ yields an acceptable—or at least not implausible—match to a set of observations z . History matching has been employed in various studies involving complex computer models [60–63] ranging, e.g., from effects of climate modeling [64, 65] to systems biology [66]. The present work represents the first application in nuclear physics.

We introduce the individual implausibility measure

$$I_i^2(\theta) = \frac{|M_i(\theta) - z_i|^2}{\text{Var}(M_i(\theta) - z_i)}, \quad (3)$$

which is a function over the input parameter space and quantifies the (mis-)match between our (emulated) model output $M_i(\theta)$ and the observation z_i for an observable in the target set \mathcal{Z} . We mainly employ a maximum implausibility measure as the restricting quantity. Specifically, we consider a particular value for θ as implausible if

$$I_M(\theta) \equiv \max_{z_i \in \mathcal{Z}} I_i(\theta) > c_I, \quad (4)$$

with $c_I \equiv 3.0$ appealing to Pukelheim’s three-sigma rule [67]. In accordance with the assumptions leading to Eq. (1), the variance in the denominator of Eq. (3) is a sum of independent squared errors. Generalizations

of these assumptions are straightforward if additional information on error covariances or possible inaccuracies in our error model would become available.

An important strength of the history matching is that we can proceed iteratively, excluding regions of input space by imposing cutoffs on implausibility measures that can include *additional* observables z_i and corresponding model outputs M_i with possibly refined emulators as the parameter volume is reduced. The iterative history matching proceeds in waves according to a straightforward strategy that can be summarized as follows:

1. At wave j : Evaluate a set of model runs over the current NI volume \mathcal{Q}_j using a space-filling design of sample values for the parameter inputs θ . Choose a rejection strategy based on implausibility measures for a set \mathcal{Z}_j of informative observables.
2. Construct or refine emulators for the model predictions across \mathcal{Q}_j .
3. The implausibility measures are then calculated over \mathcal{Q}_j using the emulators, and implausibility cutoffs are imposed. This defines a new, smaller non-implausible volume \mathcal{Q}_{j+1} which should satisfy $\mathcal{Q}_{j+1} \subset \mathcal{Q}_j$.
4. Unless (a) computational resources are exhausted, or (b) all considered points in the parameter space are deemed implausible, we may include additional informative observables in the considered set \mathcal{Z}_{j+1} , and return to step 1.
5. If 4(a) is true we generate a number of acceptable runs from the final non-implausible volume $\mathcal{Q}_{\text{final}}$, sampled according to scientific need.

The *ab initio* model for the observables we consider comprises at most 17 parameters; four subleading pion-nucleon couplings, 11 nucleon-nucleon contact couplings, and two short-ranged three-nucleon couplings. To identify a set of non-implausible parameter samples we performed iterative history matching in four waves using observables and implausibility measures as summarized in Extended Data Figure 4b. For each wave we employ a sufficiently dense Latin hypercube set of several million candidate parameter samples. For the model evaluations we utilized fast computations of neutron-proton scattering phase shifts and efficient emulators for the few- and many-body history-matching observables. See Extended Data Table 1 and Extended Data Figure 5 for the list of history-matching observables and information on the errors that enter the implausibility measure (3). The input volume for wave 1 incorporates the naturalness expectation for LECs, but still includes large ranges for the relevant parameters as indicated by the panel ranges in Extended Data Figure 4a. In all four waves the input volume for $c_{1,2,3,4}$ is a four-dimensional hypercube

mapped onto the multivariate Gaussian probability density function (PDF) resulting from a Roy-Steiner analysis of pion-nucleon scattering data [68]. In wave 1 and wave 2 we sampled all relevant parameter directions for the set of included two-nucleon observables. In wave 3, the ^3H and ^4He observables were added such that the three-nucleon force parameters c_D and c_E can also be constrained. Since these observables are known to be rather insensitive to the four model parameters acting solely in P -waves, we ignored this subset of the inputs and compensated by slightly enlarging the corresponding method errors. This is a well known emulation procedure called inactive parameter identification [21]. For wave 4 we considered all 17 model parameters and added the energy and radius of ^{16}O to the set \mathcal{Z}_4 and emulated the model outputs for 5×10^8 parameter samples. Extended Data Figure 4a summarizes the sequential non-implausible volume reduction, wave-by-wave, and indicates the set of 4,337 non-implausible samples after the fourth wave. The volume reduction is determined by the maximum implausibility cutoff (4) with additional information from the optical depths (see Eqs. (25) and (26) in Ref. [66]). The non-implausible samples summarise the parameter region of interest, and can directly aid insight regarding interdependencies between parameters induced by the match to observed data. This region is also where we would expect the posterior distribution to reside and we note that our history-matching procedure has allowed us to reduce its size by more than seven orders of magnitude compared to the prior volume (see Extended Data Figure 4b).

As a final step, we confront the set of non-implausible samples from wave 4 with neutron-proton scattering phase shifts such that our final set of non-implausible samples has been matched with all history-matching observables. For this final implausibility check we employ a slightly less strict cutoff and allow the first, second and third maxima of $I_i(\theta)$ (for $z_i \in \mathcal{Z}_{\text{final}}$) to be 5.0, 4.0, and 3.0, respectively, accommodating the more extreme maxima we may anticipate when considering a significantly larger number of observables. The end result is a set of 34 non-implausible samples that we use for predicting ^{48}Ca and ^{208}Pb observables, as well as the equation of state of both symmetric nuclear matter and pure neutron matter.

Posterior predictive distributions

The 34 non-implausible samples from the final history matching wave are used to compute energies, radii of proton and neutron distributions, and electric dipole polarizabilities (α_D) for ^{48}Ca and ^{208}Pb . They are also used to compute the electric and weak charge form factors for the same nuclei at a relevant momentum transfer, and the energy per particle of infinite nuclear matter at various densities to extract key properties of the nuclear equation of state (see below). These results are shown as blue

circles in Figure 3.

In order to make quantitative predictions, with a statistical interpretation, for $R_{\text{skin}}(^{208}\text{Pb})$ and other observables we use the same 34 parameter sets to extract representative samples from the posterior PDF $p(\theta|\mathcal{D}_{\text{cal}})$. Bulk properties (energies and charge radii) of ^{48}Ca together with the structure-sensitive 2^+ excited-state energy of ^{48}Ca are used to define the calibration data set \mathcal{D}_{cal} . The IMSRG and CC convergence studies make it possible to quantify the method errors. These are summarized in Extended Data Table 1. The EFT truncation errors are quantified by adopting the EFT convergence model [69, 70] for observable y

$$y = y_{\text{ref}} \left(\sum_{i=0}^k c_i Q^i + \sum_{i=k+1}^{\infty} c_i Q^i \right), \quad (5)$$

with observable coefficients c_i that are expected to be of natural size, and the expansion parameter $Q = 0.42$ following our Bayesian error model for nuclear matter at the relevant density (see below). The first sum in the parenthesis is the model prediction $y_k(\theta)$ of observable y at truncation order k in the chiral expansion. The second sum then represents the model error as it includes the terms that are not explicitly included. We can quantify the magnitude of these terms by learning about the distribution for c_i which we will assume is described by a single normal distribution per observable type with zero mean and a variance parameter \bar{c}^2 . We employ the nuclear matter error analysis for the energy per particle of symmetric nuclear matter (described below) to provide the model error for E/A in ^{48}Ca and ^{208}Pb . For radii and electric dipole polarizabilities we employ the next-to-leading order and next-to-next-to leading order interactions of Ref. [56] and compute these observables at both orders for various Ca, Ni, and Sn isotopes. The reference values y_{ref} are set to $r_0 \cdot A^{1/3}$ for radii and to the experimental value for α_D . From this data we extract \bar{c}^2 and perform the geometric sum of the second term in Eq. (5). The resulting standard deviations for model errors are summarized in Extended Data Table 1.

At this stage we can extract samples from the parameter posterior by assuming a uniform prior probability for the non-implausible samples, and a normally distributed likelihood with independent experimental, method, and model errors, by employing importance resampling [33]:[71]. Note, however, that the prior for $c_{1,2,3,4}$ is the multivariate Gaussian resulting from a Roy-Steiner analysis of πN scattering data [68].

Although we are operating with a finite number of 34 representative samples from the parameter PDF, it is reassuring that about half of them are within a factor two from the most probable one in terms of the importance weight. Consequently, our final predictions will not be dominated by a very small number of interactions. We use these samples to draw corresponding samples from

$$\text{PPD}_{\text{parametric}} = \{y_k(\theta) : \theta \sim p(\theta|\mathcal{D}_{\text{cal}})\}. \quad (6)$$

This posterior predictive distribution (PPD) is the set of all model predictions computed over likely values of the parameters, i.e., drawing from the posterior PDF for θ . The full PPD is then defined, in analogy with Eq. (6), as the set evaluation of y which is the sum

$$y = y_k + \epsilon_{\text{method}} + \epsilon_{\text{model}}, \quad (7)$$

where we assume method and model errors to be independent of the parameters. In practice, we produce 10^4 samples from this full PPD for y by resampling the 34 samples of the model PPD (6) according to their importance weights, and adding samples from the error terms in (7). We perform model checking by comparing this final PPD with the data used in the iterative history-matching step, and in the likelihood calibration. In addition, we find that our predictions for the the measured electric dipole polarizabilities of ^{48}Ca and ^{208}Pb as well as bulk properties of ^{208}Pb serve as a validation of the reliability of our analysis and assigned errors. See Figure 2 and Extended Data Table 1.

In addition, we explored the sensitivity of our results to modifications of the likelihood definition. Specifically, we used a student-t distribution ($\nu = 5$) to see the effects of allowing heavier tails, and we introduced an error covariance matrix to study the effect of possible correlations (with $\rho \approx 0.7$) between the errors in binding energy and radius of ^{48}Ca . In the end, the differences in the extracted credibility regions was $\sim 1\%$ and we therefore present only results obtained with the uncorrelated, multivariate normal distribution.

Our final predictions for $R_{\text{skin}}(^{208}\text{Pb})$, $R_{\text{skin}}(^{48}\text{Ca})$ and for nuclear matter properties are presented in Figure 3 and Extended Data Table 2. For these observables we use the Bayesian machine learning error model described below to assign relevant correlations between equation-of-state observables. For model errors in $R_{\text{skin}}(^{208}\text{Pb})$ and L we use a correlation coefficient of $\rho = 0.9$ as motivated by the strong correlation between the observables computed with the 34 non-implausible samples.

Bayesian machine learning error model

Similar to Eq. (1) the predicted nuclear matter observables can be written as:

$$y = y_k(\rho) + \epsilon_k(\rho) + \epsilon_{\text{method}}(\rho). \quad (8)$$

where $y_k(\rho)$ is the CC prediction using our EFT model truncated at order k , $\epsilon_k(\rho)$ is the EFT truncation (model) error, and $\epsilon_{\text{method}}(\rho)$ is the CC method error. In this work we apply a Bayesian machine learning error model [35] to quantify the density dependence of both method and truncation errors. The error model is based on multitask Gaussian processes that learn both the size and the correlations of the target errors from given prior information. Following a physically-motivated Gaussian

process (GP) model [35], the EFT truncation errors ϵ_k at given density ρ are distributed as:

$$\epsilon_k(\rho) \mid \bar{c}^2, l, Q \sim \text{GP}[0, \bar{c}^2 R_{\epsilon_k}(\rho, \rho'; l)], \quad (9)$$

with

$$R_{\epsilon_k}(\rho, \rho'; l) = y_{\text{ref}}(\rho) y_{\text{ref}}(\rho') \frac{[Q(\rho)Q(\rho')]^{k+1}}{1 - Q(\rho)Q(\rho')} r(\rho, \rho'; l). \quad (10)$$

Here $k = 3$ for the $\Delta\text{NNLO}(394)$ EFT model used in this work, while \bar{c}^2 , l and Q are hyperparameters corresponding to the variance, the correlation length, and the expansion parameter. Finally, we choose the reference scale y_{ref} to be the EFT leading-order prediction. The mean of the Gaussian process is set to be zero since the order-by-order truncation error can either be positive or negative and the correlation function $r(\rho, \rho'; l)$ in (10) is the Gaussian radial basis function.

We employ Bayesian inference to optimize the Gaussian process hyperparameters using order-by-order predictions of the equation of state for both pure neutron matter and symmetric nuclear matter with the Δ -full interactions from Ref. [59]. In this work, we find $\bar{c}_{\text{PNM}} = 1.00$ and $l_{\text{PNM}} = 0.92 \text{ fm}^{-1}$ for pure neutron matter and $\bar{c}_{\text{SNM}} = 1.55$ and $l_{\text{SNM}} = 0.48 \text{ fm}^{-1}$ for symmetric nuclear matter.

The above Gaussian processes only describe the correlated structure of truncation errors for one type of nucleonic matter. In addition, the correlation between pure neutron matter and symmetric nuclear matter is crucial for correctly assigning errors to observables that involve both E/N and E/A (such as the symmetry energy S). For this purpose we use a multitask Gaussian process that simultaneously describes truncation errors of pure neutron matter and symmetric nuclear matter according to:

$$\begin{bmatrix} \epsilon_{k,\text{PNM}} \\ \epsilon_{k,\text{SNM}} \end{bmatrix} \sim \text{GP} \left(\begin{bmatrix} 0 \\ 0 \end{bmatrix}, \begin{bmatrix} K_{11} & K_{12} \\ K_{21} & K_{22} \end{bmatrix} \right), \quad (11)$$

where K_{11} and K_{22} are the covariance matrices generated from the kernel function $\bar{c}^2 R_{\epsilon_k}(\rho, \rho'; l)$ for pure neutron matter and symmetric nuclear matter, respectively, while $K_{12}(K_{21})$ is the cross-covariance as in Ref. [72].

Moreover, we use a similar approach to also learn the CC method errors which, however, does not share the same order-by-order structure as the EFT truncation error. On the other hand, we can employ convergence studies of the CC method to train the following Bayesian error model:

$$\epsilon_{\text{method}}(\rho) \mid \bar{c}_{\text{me}}^2, l_{\text{me}}, \sim \text{GP}[0, \bar{c}_{\text{me}}^2 R_{\text{me},\delta k}(\rho, \rho'; l_{\text{me}})], \quad (12)$$

with

$$R_{\text{me},\delta k}(\rho, \rho'; l_{\text{me}}) = y_{\text{me,ref}}(\rho) y_{\text{me,ref}}(\rho') r(\rho, \rho'; l_{\text{me}}). \quad (13)$$

Here the reference scale $y_{\text{me,ref}}$ is taken to be the CCD(T) correlation energy. The Gaussian processes are then

trained with data from different interactions by assuming that the energy difference between CCD(T) and CCD can be used as an approximation of the CC method error. The correlation lengths learned from the training data are $l_{\text{me,PNM}} = 0.81 \text{ fm}^{-1}$ for pure neutron matter and $l_{\text{me,SNM}} = 0.34 \text{ fm}^{-1}$ for symmetric nuclear matter. We take $\bar{c}_{\text{me}} = 0.05$ based on a convergence study of the energy difference between CCD(T) and CCD method truncations.

Once the multitask Gaussian processes of the model and method errors are determined, it is straightforward to sample these errors from the corresponding covariance matrix and produce the equation-of-state predictions using Eq. (8) for any given interaction. This sampling procedure is crucial for generating the posterior predictive distribution of nuclear matter observables shown in Figure 3a. CCD(T) calculations for nuclear-matter equation of state and the corresponding 2σ credible interval for method and model errors are illustrated in Extended Data Figure 6. The sampling procedure is made explicit with three randomly sampled equation-of-state predictions. Note that even though the sampled errors for one given density appear to be random, the multitask Gaussian processes will guarantee that the sampled equation of state of nuclear matter are smooth and properly correlated with each other.

-
- [44] G. Hagen, T. Papenbrock, D. J. Dean, A. Schwenk, A. Nogga, M. Włoch, and P. Piecuch, *Phys. Rev. C* **76**, 034302 (2007).
- [45] R. Roth, S. Binder, K. Vobig, A. Calci, J. Langhammer, and P. Navrátil, *Phys. Rev. Lett.* **109**, 052501 (2012).
- [46] K. Tsukiyama, S. K. Bogner, and A. Schwenk, *Phys. Rev. Lett.* **106**, 222502 (2011).
- [47] T. D. Morris, N. M. Parzuchowski, and S. K. Bogner, *Phys. Rev. C* **92**, 034331 (2015).
- [48] N. M. Parzuchowski, S. R. Stroberg, P. Navrátil, H. Hergert, and S. K. Bogner, *Phys. Rev. C* **96**, 034324 (2017), arXiv:1705.05511.
- [49] M. Miorelli, S. Bacca, N. Barnea, G. Hagen, G. R. Jansen, G. Orlandini, and T. Papenbrock, *Phys. Rev. C* **94**, 034317 (2016).
- [50] P.-G. Reinhard, J. Piekarewicz, W. Nazarewicz, B. K. Agrawal, N. Paar, and X. Roca-Maza, *Phys. Rev. C* **88**, 034325 (2013).
- [51] M. Hoferichter, J. Menéndez, and A. Schwenk, *Phys. Rev. D* **102**, 074018 (2020), arXiv:2007.08529.
- [52] A. G. Taube and R. J. Bartlett, *J. Chem. Phys.* **128**, 044110 (2008).
- [53] J. F. Stanton and R. J. Bartlett, *J. Chem. Phys.* **98**, 7029 (1993).
- [54] G. Hagen, G. R. Jansen, and T. Papenbrock, *Phys. Rev. Lett.* **117**, 172501 (2016).
- [55] J. Noga, R. J. Bartlett, and M. Urban, *Chem. Phys. Lett.* **134**, 126 (1987).
- [56] W. G. Jiang, A. Ekström, C. Forssén, G. Hagen, G. R. Jansen, and T. Papenbrock, *Phys. Rev. C* **102**, 054301 (2020).
- [57] S. Wesolowski, N. Klco, R. Furnstahl, D. Phillips, and A. Thapaliya, *J. Phys. G* **43**, 074001 (2016), arXiv:1511.03618 [nucl-th].
- [58] J. Melendez, S. Wesolowski, and R. Furnstahl, *Phys. Rev. C* **96**, 024003 (2017), arXiv:1704.03308 [nucl-th].
- [59] A. Ekström, G. Hagen, T. D. Morris, T. Papenbrock, and P. D. Schwartz, *Phys. Rev. C* **97**, 024332 (2018).
- [60] P. S. Craig, M. Goldstein, A. H. Seheult, and J. A. Smith, in *Bayesian Statistics 5*, edited by J. M. Bernardo, J. O. Berger, A. P. Dawid, and A. F. M. Smith (Clarendon Press, Oxford, UK, 1996) p. 69.
- [61] P. S. Craig, M. Goldstein, A. H. Seheult, and J. A. Smith, in *Case Studies in Bayesian Statistics*, Vol. 3, edited by C. Gatsonis, J. S. Hodges, R. E. Kass, R. McCulloch, P. Rossi, and N. D. Singpurwalla (New York, 1997) p. 36.
- [62] I. Vernon, M. Goldstein, and R. G. Bower, *Bayesian Anal.* **5**, 697 (2010).
- [63] I. Andrianakis, I. R. Vernon, N. McCreesh, T. J. McKinley, J. E. Oakley, R. N. Nsubuga, M. Goldstein, and R. G. White, *PLoS Comput Biol.* **11**, e1003968 (2015).
- [64] D. Williamson, M. Goldstein, L. Allison, A. Blaker, P. Challenor, L. Jackson, and K. Yamazaki, *Clim. Dyn.* **41**, 1703 (2013).
- [65] T. L. Edwards, M. A. Brandon, G. Durand, N. R. Edwards, N. R. Golledge, P. B. Holden, I. J. Nias, A. J. Payne, C. Ritz, and A. Wernecke, *Nature* **566**, 58 (2019).
- [66] I. Vernon, J. Liu, M. Goldstein, J. Rowe, J. Topping, and K. Lindsey, *BMC Systems Biology* **12**, 1 (2018).
- [67] F. Pukelshim, *Am. Stat.* **48**, 88 (1994).
- [68] D. Siemens, J. Ruiz de Elvira, E. Epelbaum, M. Hoferichter, H. Krebs, B. Kubis, and U.-G. Meißner, *Phys. Lett. B* **770**, 27 (2017).
- [69] R. J. Furnstahl, N. Klco, D. R. Phillips, and S. Wesolowski, *Phys. Rev. C* **92**, 024005 (2015).
- [70] J. A. Melendez, R. J. Furnstahl, D. R. Phillips, M. T. Pratala, and S. Wesolowski, *Phys. Rev. C* **100**, 044001 (2019), arXiv:1904.10581 [nucl-th].
- [71] J. Bernardo and A. Smith, *Bayesian Theory*, Wiley Series in Probability and Statistics (John Wiley & Sons Canada, Limited, 2006).
- [72] C. Drischler, J. A. Melendez, R. J. Furnstahl, and D. R. Phillips, *Phys. Rev. C* **102**, 054315 (2020), arXiv:2004.07805 [nucl-th].
- [73] R. N. Pérez, J. E. Amaro, and E. R. Arriola, *Phys. Rev. C* **88**, 064002 (2013).
- [74] M. Wang, W. J. Huang, F. G. Kondev, G. Audi, and S. Naimi, *Chin. Phys. C* **45**, 030003 (2021).
- [75] L. Multhauf, K. Tirsell, S. Raman, and J. McGrory, *Phys. Lett. B* **57**, 44 (1975).
- [76] I. Angeli and K. Marinova, *At. Data Nucl. Data Tables* **99**, 69 (2013).
- [77] B. D. Carlsson, A. Ekström, C. Forssén, D. F. Strömberg, G. R. Jansen, O. Lilja, M. Lindby, B. A. Mattsson, and K. A. Wendt, *Phys. Rev. X* **6**, 011019 (2016), arXiv:1506.02466 [nucl-th].
- [78] R. Machleidt, *Phys. Rev. C* **63**, 024001 (2001).
- [79] J. Birkhan, M. Miorelli, S. Bacca, S. Bassauer, C. A. Bertulani, G. Hagen, H. Matsubara, P. von Neumann-Cosel, T. Papenbrock, N. Pietralla, V. Y. Ponomarev, A. Richter, A. Schwenk, and A. Tamii, *Phys. Rev. Lett.* **118**, 252501 (2017).
- [80] A. Tamii, I. Poltoratska, P. von Neumann-Cosel, Y. Fujita, T. Adachi, C. A. Bertulani, J. Carter, M. Dozono, H. Fujita, K. Fujita, K. Hatanaka, D. Ishikawa,

- M. Itoh, T. Kawabata, Y. Kalmykov, A. M. Krumbholz, E. Litvinova, H. Matsubara, K. Nakanishi, R. Neveling, H. Okamura, H. J. Ong, B. Özel-Tashenov, V. Y. Ponomarev, A. Richter, B. Rubio, H. Sakaguchi, Y. Sakemi, Y. Sasamoto, Y. Shimbara, Y. Shimizu, F. D. Smit, T. Suzuki, Y. Tameshige, J. Wambach, R. Yamada, M. Yosoi, and J. Zenihiro, *Phys. Rev. Lett.* **107**, 062502 (2011).
- [81] M. Bender, P.-H. Heenen, and P.-G. Reinhard, *Rev. Mod. Phys.* **75**, 121 (2003).
- [82] S. Shlomo, V. Kolomietz, and G. Colo, *Eur. Phys. J. A* **30**, 23 (2006).
- [83] B. A. Brown and B. H. Wildenthal, *Ann. Rev. Nucl. Part. Sci.* **38**, 29 (1988).
- [84] D. Vautherin and D. M. Brink, *Phys. Rev. C* **5**, 626 (1972), 0711.0106.
- [85] M. Beiner, H. Flocard, N. Van Giai, and P. Quentin, *Nucl. Physics, Sect. A* **238**, 29 (1975).
- [86] H. S. Köhler, *Nucl. Physics, Sect. A* **258**, 301 (1976).
- [87] P. G. Reinhard and H. Flocard, *Nucl. Physics, Sect. A* **584**, 467 (1995).
- [88] F. Tondeur, M. Brack, M. Farine, and J. Pearson, *Nucl. Phys. A* **420**, 297 (1984).
- [89] J. Dobaczewski, H. Flocard, and J. Treiner, *Nucl. Phys. A* **422**, 103 (1984).
- [90] N. Van Giai and H. Sagawa, *Phys. Lett. B* **106**, 379 (1981).
- [91] M. M. Sharma, G. Lalazissis, J. König, and P. Ring, *Phys. Rev. Lett.* **74**, 3744 (1995).
- [92] P. G. Reinhard, D. J. Dean, W. Nazarewicz, J. Dobaczewski, J. A. Maruhn, and M. R. Strayer, *Phys. Rev. C* **60**, 20 (1999).
- [93] J. Bartel, P. Quentin, M. Brack, C. Guet, and H. B. Håkansson, *Nucl. Phys. A* **386**, 79 (1982)

Data availability

The data that support the plots within this paper and other findings of this study are available from the corresponding author upon reasonable request.

Code availability

Our unpublished computer codes used to generate results that are reported in the paper and central to its main claims will be made available upon request, to editors and reviewers. The code used

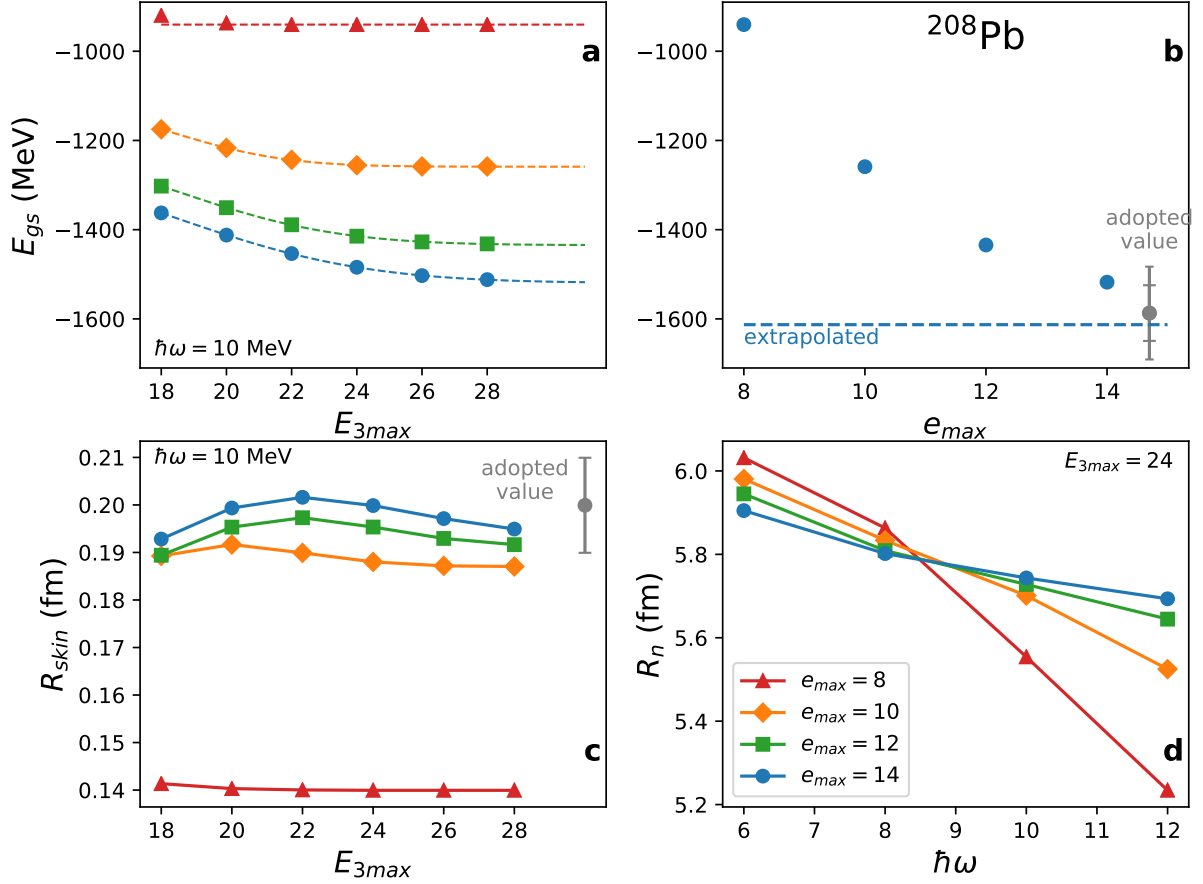
to perform the IMSRG calculations is available at <https://github.com/ragnarstroberg/imsrg>.

Acknowledgements

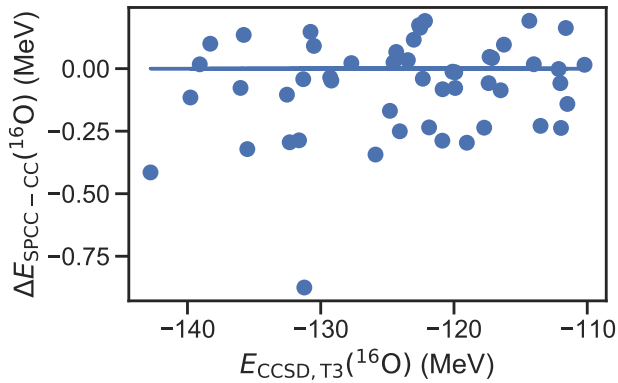
This material is based upon work supported by the Swedish Research Council grant number 2017-04234, the European Research Council (ERC) under the European Union’s Horizon 2020 research and innovation programme (grant agreement number 758027), the U.S. Department of Energy, Office of Science, Office of Nuclear Physics under award numbers DE-FG02-96ER40963 and DE-SC0018223 (NUCLEI SciDAC-4 collaboration), the Natural Sciences and Engineering Research Council of Canada under grants SAPIN-2018-00027 and RGPAS-2018-522453, and the Arthur B. McDonald Canadian Astroparticle Physics Research Institute. TRIUMF receives funding via a contribution through the National Research Council of Canada. Computer time was provided by the Innovative and Novel Computational Impact on Theory and Experiment (INCITE) programme. This research used resources of the Oak Ridge Leadership Computing Facility located at Oak Ridge National Laboratory, which is supported by the Office of Science of the Department of Energy under contract No. DE-AC05-00OR22725, and resources provided by the Swedish National Infrastructure for Computing (SNIC) at Chalmers Centre for Computational Science and Engineering (C3SE), and the National Supercomputer Centre (NSC) partially funded by the Swedish Research Council, as well as Cedar at West-Grid and Compute Canada.

Author contributions

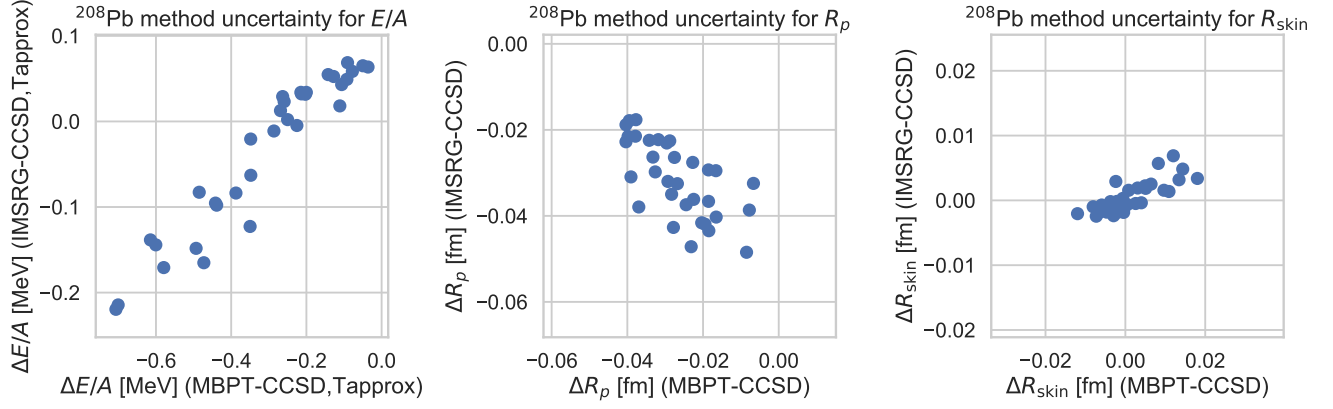
C.F. led the project. G.H., T.P., W.G.J., and Z.S. performed coupled-cluster computations. A.E., C.F., W.G.J., and I.V. designed and conducted the history-matching runs, A.E., C.F., W.G.J., S.R.S., and I.V. carried out the statistical analysis. B.S.H., T.M., J.D.H., and S.R.S. performed in-medium similarity renormalization group calculations. All authors aided in writing the manuscript.



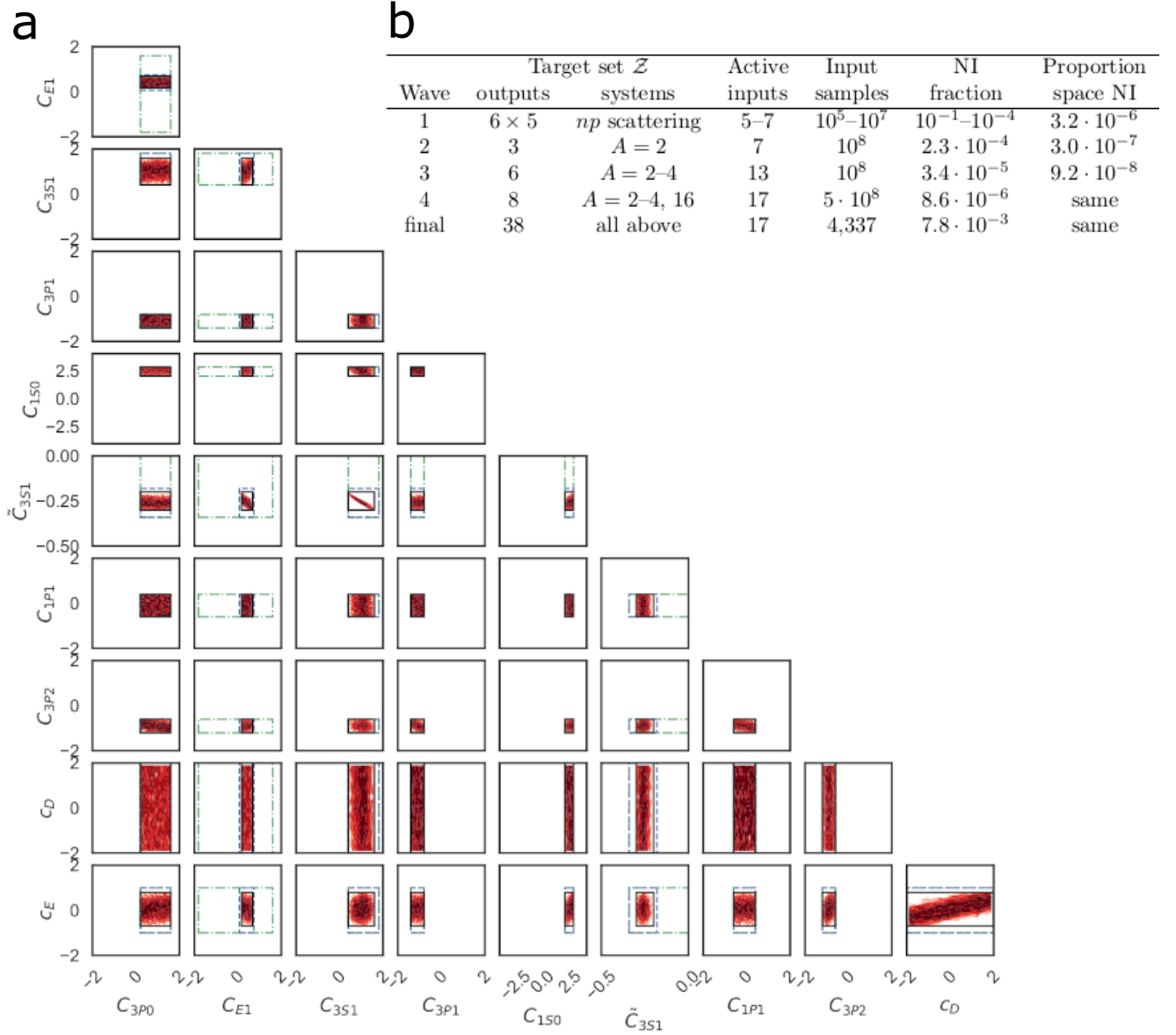
Extended Data Figure 1 | Convergence of energy and radius observables of ^{208}Pb with the e_{max} and E_{3max} truncations. **a**, Ground state energy as a function of E_{3max} . The dashed lines indicate a Gaussian fit. **b**, Ground state energy (extrapolated in E_{3max} as a function of e_{max}). The smaller error bar on the adopted value indicate the error due to model space extrapolation, and the larger error bar also includes the method uncertainty. **c**, Neutron skin as a function of E_{3max} . **d**, Neutron radius as a function of oscillator basis frequency $\hbar\omega$ for a series of e_{max} cuts.



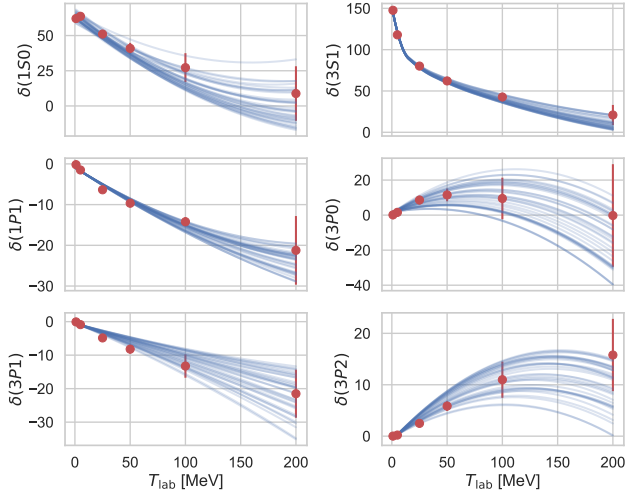
Extended Data Figure 2 | **Sub-space coupled-cluster method.** Cross-validation of the SP-CCSDT-3 emulator for the ground-state energy of ^{16}O . Results from full computations using CCSDT-3 are compared with emulator predictions for 50 samples from the 17 dimensional space of LECs. The standard deviation for the residuals is 0.19 MeV.



Extended Data Figure 3 | Precision of many-body solvers. Differences between IMSRG and CC results versus differences between MBPT and CC results for the ground-state energy (left panel), the point-proton radius (middle panel), and the neutron-skin (right panel) of ^{208}Pb using the 34 non-implausible interactions obtained from history matching (see text for more details). The CC results for the ground-state energy include approximate triples corrections.



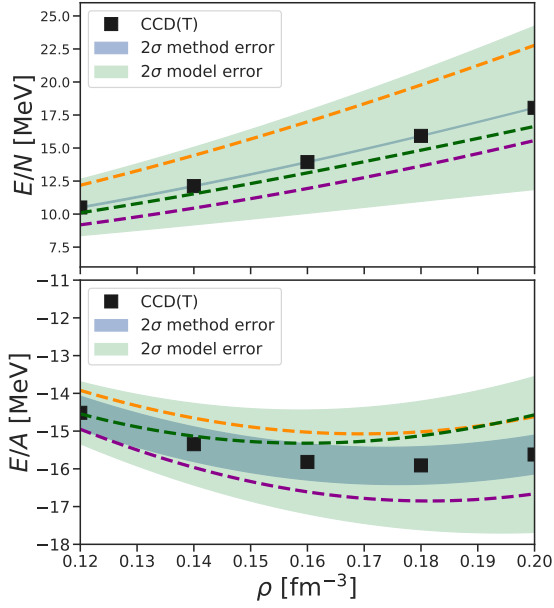
Extended Data Figure 4 | History-matching waves. **a**, The initial parameter domain used at the start of history-matching wave 1 is represented by the axes limits for all panels. This domain is iteratively reduced and the input volumes of waves 2, 3, and 4 are indicated by green/dash-dotted, blue/dashed, black/solid rectangles. The optical depths (indicating the density of non-implausible samples) in the final wave are shown in red with darker regions corresponding to a denser distribution of non-implausible samples. **b**, Four waves of history matching were used in this work plus a fifth one to refine the final set of non-implausible samples. The neutron-proton scattering targets correspond to phase shifts at six energies ($T_{\text{lab}} = 1, 5, 25, 50, 100, 200$ MeV) per partial wave: $^1S_0, ^3S_1, ^1P_1, ^3P_0, ^3P_1, ^3P_2$. The $A = 2$ observables are $E(^2\text{H}), R_p(^2\text{H}), Q(^2\text{H})$, while $A = 3, 4$ are $E(^3\text{H}), E(^4\text{He}), R_p(^4\text{He})$. Finally, $A = 16$ targets are $E(^{16}\text{O}), R_p(^{16}\text{O})$. The number of active input parameters is indicated in the fourth column. The number of inputs sets being explored, and the fraction of non-implausible samples that survive the imposed implausibility cutoff(s) are shown in the fifth and sixth columns, respectively. Finally, the proportion of the parameter space deemed non implausible is listed in the last column. Note that no additional reduction of the non-implausible domain is performed in the fourth and final waves.



Extended Data Figure 5 | Neutron-proton scattering phase shifts. 34 interaction samples survive the final implausibility cutoff with respect to neutron-proton phase shifts in S and P waves up to 200 MeV. The red circles are from the Granada phase shift analysis[73], while the 2σ error bars are dominated by the estimated EFT truncation errors[59].

Extended Data Table 1 | Error assignments, PPD model checking and validation. Experimental target values and error assignments for observables used in the fourth wave of the iterative history matching (history-matching observables), for the Gaussian likelihood calibration of the final non-implausible samples (calibration observables), and for model validation with predicted ^{208}Pb observables and electric dipole polarizabilities (validation observables). Energies (in MeV) with experimental targets from Refs. [74, 75], point-proton radii (in fm) with experimental targets translated from measured charge radii [76] (see Ref. [77] for more details). For the deuteron quadrupole moment (in $e^2\text{fm}^2$) we use the theoretical result obtained from the high-precision meson-exchange nucleon-nucleon model CD-Bonn[78] as a target with a 4% error bar. Electric dipole polarizability α_D (in fm^3) with experimental targets from Refs. [79, 80]. Theoretical model (method) errors are estimated from the EFT (many-body) convergence pattern as discussed in the text. These theory errors have zero mean except for $E_{2+}(^{48}\text{Ca})$ with $\mu_{\text{method}} = -1$ MeV from estimated triples and $E/A(^{208}\text{Pb})$ with $\mu_{\text{method}} = -0.36$ MeV/A from e_{max} extrapolation. Emulator errors are estimated from cross validation. The final prediction from the PPD described in the text (and shown in Figure 2) is summarized by the median and the 68% credibility region in the last column.

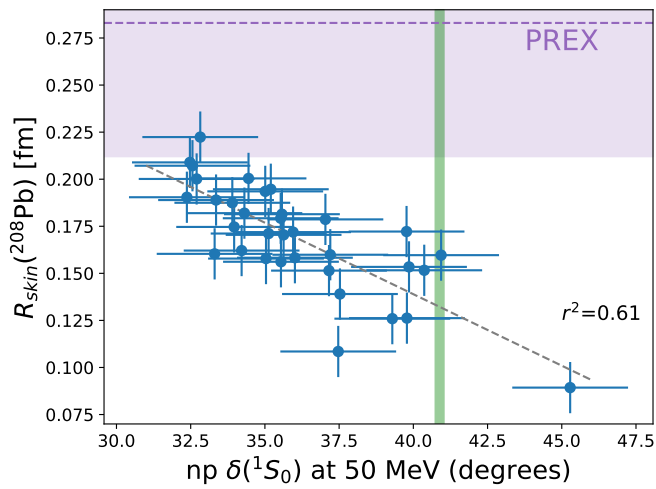
History-matching observables						
Observable	z	ε_{exp}	$\varepsilon_{\text{model}}$	$\varepsilon_{\text{method}}$	ε_{em}	PPD
$E(^2\text{H})$	-2.2246	0.0	0.05	0.0005	0.001%	$-2.22^{+0.07}_{-0.07}$
$R_p(^2\text{H})$	1.976	0.0	0.005	0.0002	0.0005%	$1.98^{+0.01}_{-0.01}$
$Q(^2\text{H})$	0.27	0.01	0.003	0.0005	0.001%	$0.28^{+0.02}_{-0.02}$
$E(^3\text{H})$	-8.4821	0.0	0.17	0.0005	0.01%	$-8.54^{+0.34}_{-0.37}$
$E(^4\text{He})$	-28.2957	0.0	0.55	0.0005	0.01%	$-28.86^{+0.86}_{-1.01}$
$R_p(^4\text{He})$	1.455	0.0	0.016	0.0002	0.003%	$1.47^{+0.03}_{-0.03}$
$E(^{16}\text{O})$	127.62	0.0	1.0	0.75	0.5%	$-126.2^{+3.0}_{-2.8}$
$R_p(^{16}\text{O})$	2.58	0.0	0.03	0.01	0.5%	$2.57^{+0.06}_{-0.06}$
Calibration observables						
Observable	z	ε_{exp}	$\varepsilon_{\text{model}}$	$\varepsilon_{\text{method}}$	ε_{em}	PPD
$E/A(^{48}\text{Ca})$	-8.667	0.0	0.54	0.25	—	$-8.58^{+0.72}_{-0.72}$
$E_{2+}(^{48}\text{Ca})$	3.83	0.0	0.5	0.5	—	$3.79^{+0.86}_{-0.96}$
$R_p(^{48}\text{Ca})$	3.39	0.0	0.11	0.03	—	$3.36^{+0.14}_{-0.13}$
Validation observables						
Observable	z	ε_{exp}	$\varepsilon_{\text{model}}$	$\varepsilon_{\text{method}}$	ε_{em}	PPD
$E/A(^{208}\text{Pb})$	-7.867	0.0	0.54	0.5	—	$-8.06^{+0.99}_{-0.88}$
$R_p(^{208}\text{Pb})$	5.45	0.0	0.17	0.05	—	$5.43^{+0.21}_{-0.23}$
$\alpha_D(^{48}\text{Ca})$	2.07	0.22	0.06	0.1	—	$2.30^{+0.31}_{-0.26}$
$\alpha_D(^{208}\text{Pb})$	20.1	0.6	0.59	0.8	—	$22.6^{+2.1}_{-1.8}$



Extended Data Figure 6 | Bayesian machine learning error model. The equation of state of pure neutron matter (top) and symmetric nuclear matter (bottom) calculated with CCD(T) (black square) are shown along with the corresponding method error (blue shade) and EFT truncation error (green shade) for one representative interaction. Note that the method error of pure neutron matter is quite small. Errors are correlated and the dashed curves illustrate predictions with randomly sampled method and model errors drawn from the respective multitask Gaussian processes. Correlations extend between pure neutron matter and symmetric nuclear matter which is represented here by curves in the same colour.

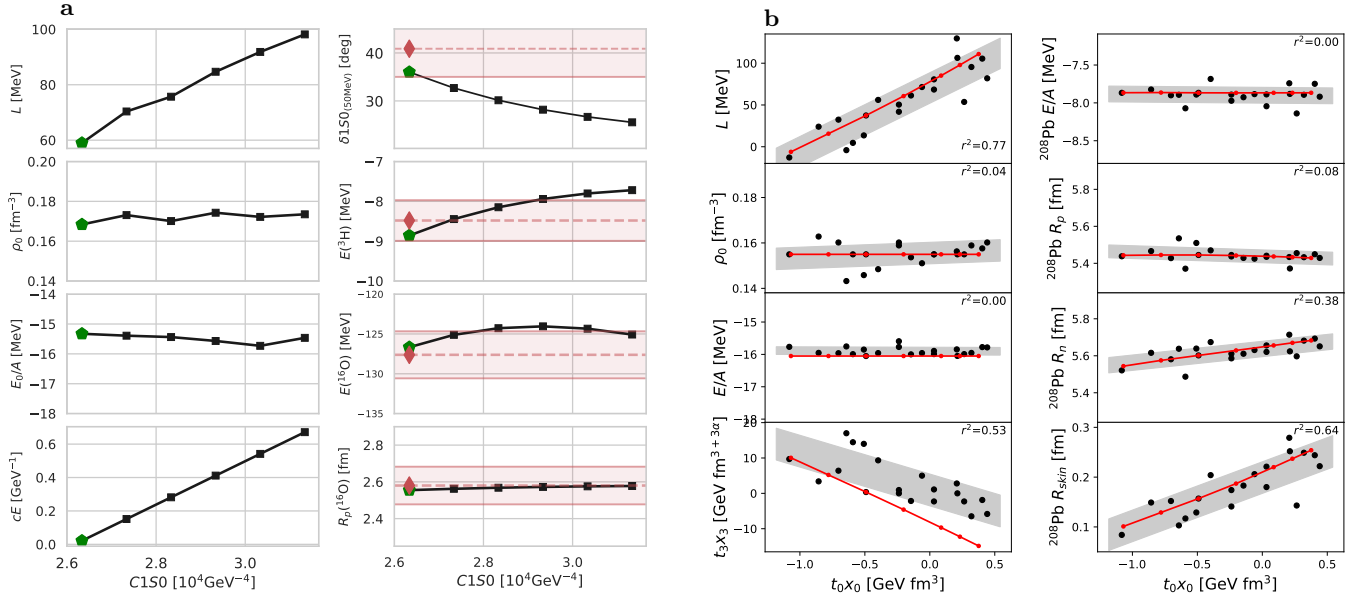
Extended Data Table 2 | Predictions for the nuclear equation of state at saturation density and for neutron skins. Medians and 68%, 90% credible regions (CR) for the final PPD including samples from the error models (see also Figure 3 and text for details). The saturation density, ρ_0 , is in (fm^{-3}), the neutron skin thickness, $R_{\text{skin}}(^{208}\text{Pb})$ and $R_{\text{skin}}(^{48}\text{Ca})$, in (fm), while the saturation energy per particle (E_0/A), the symmetry energy (S), its slope (L), and incompressibility (K) at saturation density are all in (MeV). Empirical regions shown in Figure 3 are $E_0/A = -16.0 \pm 0.5$, $\rho_0 = 0.16 \pm 0.01$, $S = 31 \pm 1$, $L = 50 \pm 10$ and $K = 240 \pm 20$ from Refs. [36]:[81, 82].

Nuclear matter properties			
Observable	median	68% CR	90% CR
E_0/A	-15.2	[-16.3, -14.0]	[-17.2, -13.5]
ρ_0	0.163	[0.147, 0.175]	[0.140, 0.186]
S	29.1	[26.6, 31.3]	[25.132.8]
L	50.3	[37.2, 68.1]	[22.6, 75.8]
K	264	[227, 297]	[210, 328]
Neutron skins			
Observable	median	68% CR	90% CR
$R_{\text{skin}}(^{48}\text{Ca})$	0.164	[0.141, 0.187]	[0.123, 0.199]
$R_{\text{skin}}(^{208}\text{Pb})$	0.171	[0.139, 0.200]	[0.120, 0.221]



Extended Data Figure 7 | Correlation between $R_{\text{skin}}(^{208}\text{Pb})$ and nucleon-nucleon scattering.

Correlation of computed $R_{\text{skin}}(^{208}\text{Pb})$ with the proton-neutron phase shift at a laboratory energy of 50 MeV, shown in blue. The error bars represent method and model (EFT) uncertainties. The green band indicates the experimental phase shift[73], while the purple band indicates the PREX result[3]. The dashed line indicates the linear trend of the *ab initio* points.



Extended Data Figure 8 | Parameter sensitivities in *ab initio* models and Skyrme parametrizations.

a, Tuning the C_{150} LEC in our *ab initio* model to adjust the symmetry energy slope parameter L while compensating with the three-nucleon contact c_E to maintain the saturation density ρ_0 and energy per nucleon E_0/A of symmetric nuclear matter. The right column shows the scattering phase shift in the 1S_0 channel at 50 MeV and observables in ^3H and ^{16}O . **b**, Illustration of the freedom in Skyrme parametrizations to adjust L while preserving ρ_0 and E_0/A . The parameters x_0, t_0, x_3, t_3 correspond to the functional form given in e.g. [83]. The black circles correspond to different parameter sets, while the red line indicates the result of starting with the SKX interaction and modifying the x_0, x_3 parameters while maintaining the binding energy of ^{208}Pb . The gray bands indicate a linear fit to the black points, with rms deviation. Skyrme parameter sets included are SKX, SKXCSB [42], SKI, SKII [84], SKIII-VI [85], SKa, SKb [86], SKI2, SKI5 [87], SKT4, SKT6 [88], SKP [89], SGI, SGII [90], MSKA [91], SKO [92], SKM* [93].